

Drop deformation and breakup in a vortex at finite inertia

By XIAOYI LI AND KAUSIK SARKAR

Department of Mechanical Engineering, University of Delaware, Newark, DE 19716, USA

(Received 23 December 2004 and in revised form 14 January 2006)

Deformation and breakup of a viscous drop in a potential vortex are numerically simulated. Capillary number, Reynolds number, and viscosity and density ratios are varied to investigate their effects on the drop dynamics. The vortex locally gives rise to an extensional flow near the drop with the axis of extension rotating at a constant rate, as the drop revolves around the vortex centre. The rotation of the axis plays a critical role in the competing dynamics between the flow-induced stretching and the interfacial tension. The relation between the rotating extensional flow and a shear flow is explored. For low capillary numbers, a periodic state is reached, where the drop deforms into an ellipsoidal shape and undergoes steady rotation with a distinct phase lag behind the imposed flow. For density-and-viscosity-matched drops, increased interfacial tension results in decreased deformation and reduced phase lag. Increased inertia promotes deformation. In the presence of inertia, decreasing capillary number leads to a negative phase lag. The rotation of the extension axis inhibits deformation at low values of the Reynolds number. But at high Reynolds numbers, rotation-induced centrifugal forces promote deformation. At low and high viscosity ratios, an increase in viscosity ratio leads to enhancement and reduction in deformation, respectively. At density ratios larger than unity, the drop deformation displays resonance in that it varies non-monotonically with a distinct peak with variation of interfacial tension and density ratio. The peak corresponds to the natural frequency of the drop deformation matching with the frequency of rotation due to the vortex. A simple physical model is used to explain various observations including asymptotic scalings. We also explore different mechanisms for drop breakup at different Reynolds number, and provide critical capillary numbers as functions of other parameters. In particular, vortex-induced resonance offers an alternative mechanism for size-selective drop breakup. Details of flow fields and transients are also presented and discussed.

1. Introduction

Drop deformation, owing to its critical importance in numerous industrial emulsions, has been extensively investigated by the fluid mechanics community. Experiments have been performed to observe isolated drops deforming in linear flows (Taylor 1932; Grace 1982; Bentley & Leal 1986). Analytical theories have been developed (Taylor 1932, 1934; Cox 1969; Frankel & Acrivos 1970; Hinch & Acrivos 1980; Rallison 1984), and detail computations performed (Youngren & Acrivos 1976; Kennedy, Pozrikidis & Skalak 1994; Loewenberg & Hinch 1996).

Much of the research on drop deformation and breakup has focused on inertialess steady Stokes flow (see reviews by Rallison (1984) and Stone (1994)). The drop

shape in such a flow is governed by the balance of viscous and interfacial tension forces, and is characterized by the capillary number and the viscosity ratio. Beyond a critical capillary number, a drop cannot achieve an equilibrium shape and breaks up into smaller droplets by dynamic processes such as end-pinching or capillary instability (Tsakalos, Navard & Peuvrel-Disdier 1998). In a steady linear flow, the drop behaviour near critical stationary states (Navot 1999; Blawdziewicz, Cristini & Loewenberg 2002) is dominated by a stable slow mode that diverges at the critical point. Stability of the drop shape depends on the flow type and its time dependence (Bentley & Leal 1986). For instance, a highly viscous drop reaches a bounded shape in a simple shear due to viscous rotation inside even for arbitrarily high capillary numbers. But for extensional flows, there is always a critical capillary number for breakup even for arbitrarily large viscosity ratios (Taylor 1932; Blawdziewicz, Cristini & Loewenberg 2003). On the other hand, transient flows such as step-shear can rupture a drop in subcritical conditions (Stone, Bentley & Leal 1986). The nonlinearity of the moving boundary problem leads to such a critical dependence on flow history. Results based on steady flow analysis therefore are not sufficient for the description of the dynamic behaviour and breakup of drops.

Inertia has also been shown to play an important role in promoting drop deformation in simple shear (Brady & Acrivos 1982; Seth & Pozrikidis 1995; Li, Renardy & Renardy 2000) and extensional flows (Kang & Leal 1987, 1989; Ramaswamy & Leal 1997). The dynamic pressure balances the interfacial forces at high inertia. Inertial drop breakup and effects of insoluble surfactants have been simulated using a volume-of-fluid (VOF) formulation (Renardy & Cristini 2001*a, b*; Renardy, Cristini & Li 2002; Khismatullin, Renardy & Cristini 2003). At high inertia, the Weber number ($We = Re Ca$) determines the dynamics, and the critical condition for breakup reaches an inviscid limit signifying a balance between the inertia and surface tension. Sarkar & Schowalter (2001*a*) investigated two-dimensional drop deformation in various time-periodic extensional flows at finite inertia and found a resonance phenomenon in the drop dynamics. The drop has a natural frequency determined by the interfacial tension and the inertia. When the frequency of the forcing flow matches the natural frequency, the drop experiences an increase in deformation. Sarkar & Schowalter (2000) also performed a two-dimensional computation of an upper-convective-Maxwell drop deforming in similar flows to find that the drop deformation varies in a complex way with the Weissenberg number due to elasticity and the presence of shear waves at finite inertia.

In this paper, we examine drop deformation and breakup in a vortex using a front-tracking finite-difference simulation (Tryggvason *et al.* 1998; Sarkar & Schowalter 2001*a*). A vortex offers an example of time-periodic flow, an important departure from steady shear and extension, and can be realized in an experiment (Hopfinger, Browand & Gagne 1982; Maxworthy, Hopfinger & Redekopp 1985). It can serve as a base flow to study the rheological response of a fluid in a non-viscometric flow. Away from the vortex centre, locally it imposes an extensional flow, with the axes of extension rotating at a fixed frequency. The effect of rotating axes on the deformation is similar to that in a steady shear which combines equal extensional and rotational contributions. Hakimi & Schowalter (1980) rightly noted that drop shapes are differently affected by the symmetric and the antisymmetric parts of the velocity gradient. We show in §2.1 that in a rotating frame, the rotating extensional flow transforms into a steady shear. However, the effects of the two flows on a finite size drop are different. The elucidation of deformation and burst mechanisms in a vortex is also important for

understanding emulsification in turbulent flows, which involve vortex structures at all length scales. Li & Sarkar (2005*a–d*) considered inertial effects on the rheology of a dilute emulsion of viscous drops in steady shear and oscillating extensional flows. Sarkar & Schowalter (2001*a, b*) briefly considered finite-inertia deformation of two-dimensional drops in a vortex along with other time-periodic extensional flows. However, they concentrated only on the resonance phenomenon for the whole class of flows. Owing to the two-dimensional nature of the computation, detailed flow structure and drop shapes were not studied. Deformation was investigated only with the Taylor criterion for elucidating the qualitative dynamics. The study was further restricted to viscosity-and-density-matched cases, which for a vortex does not allow resonance. In this paper, we provide a detailed description of the three-dimensional dynamics and flow fields inside and outside the drop in the vortex, investigate the phase relation between the drop response and the imposed flow, and extend the flow to non-unity density and viscosity ratios. Furthermore, we provide a quantitative description of the dynamics of drop breakup in a vortex.

In the following, mathematical formulation and its numerical implementation are briefly sketched. A careful convergence study is executed before the results are presented with systematic variation of parameters. A simple ordinary differential equation (ODE) model is used to explain the underlying physics.

2. Problem formulation

2.1. Kinematics of linearized vortex flow

The vortex is an irrotational flow, with each fluid element being stretched and revolving around the centre but experiencing no rotation (figure 1*a*). The principal axis of stretching rotates about the centre of the element (dashed box in figure 1*a*). For a small isolated drop away from the vortex centre, one can linearize the velocity field induced by the vortex at the drop centre. We assume that an initially spherical drop with radius R is placed at a large distance R^* from the vortex origin, $R^* \gg R$. The imposed linear flow field is

$$\begin{aligned} \mathbf{u}_0^v(\mathbf{x}) &= \mathbf{E}[\mathbf{x}_c(t)] \cdot \mathbf{x} = \mathbf{E}[R^* \cos \theta(t), R^* \sin \theta(t)] \cdot \mathbf{x} \\ &= \dot{\varepsilon}_0 \begin{pmatrix} \sin 2\theta & -\cos 2\theta \\ -\cos 2\theta & -\sin 2\theta \end{pmatrix} \cdot \begin{pmatrix} x \\ y \end{pmatrix}, \end{aligned} \quad (2.1)$$

where $\mathbf{E}[\mathbf{x}_c(t)]$ is the velocity gradient tensor evaluated at the drop centre $\mathbf{x}_c(t) = \{R^* \cos \theta(t), R^* \sin \theta(t)\}$. The magnitude of stretching is $\dot{\varepsilon}_0 = \gamma/(2\pi R^{*2})$, γ being the circulation of the vortex. The centre of the drop \mathbf{x}_c revolves around the vortex with the circular velocity $V_\theta = \gamma/(2\pi R^*)$, and the position is denoted by $\theta(t) = 2\pi t/T = \omega t/2$, where T is the period of circulation. The angular frequency ω is related to the strain rate $\dot{\varepsilon}_0$ by $\omega = 4\pi/T = 2V_r/R^* = \gamma/(\pi R^{*2}) = 2\dot{\varepsilon}_0$. Note that the frequency of local stretching is twice the frequency of the vortex due to the symmetry of opposite points across the vortex. Note also that although the flow is defined in the (x, y) -plane, the presence of the drop introduces a velocity component in the third dimension orthogonal to the plane. The flow perturbation leads to vorticity generation in the irrotational imposed flow.

Note that on going to a rotating frame,

$$\mathbf{x}' = \mathbf{Q}(t)\mathbf{x}, \quad \text{with } \mathbf{Q}(t) = \begin{pmatrix} \cos \alpha t & \sin \alpha t \\ -\sin \alpha t & -\cos \alpha t \end{pmatrix},$$

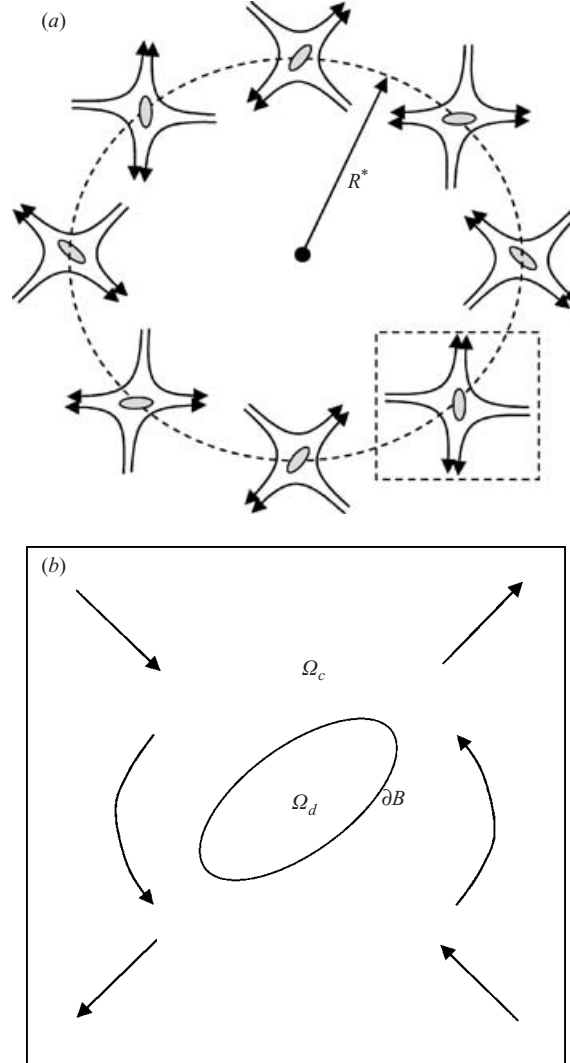


FIGURE 1. (a) Stretching of a drop with a rotating axis of stretching in vortex. The dashed circle represents the rotating path of a drop in a vortex. The arrows denote the stretching of the drop at different locations in the rotating path. (b) Schematic of domain of calculation.

the velocity gradient tensor changes as

$$\mathbf{E}' = \dot{\mathbf{Q}}\mathbf{Q}^T + \mathbf{Q}\mathbf{E}\mathbf{Q}^T.$$

In a frame rotating with the same frequency as that due to the vortex or half the frequency of axes rotation, i.e. $\alpha = \omega/2 = \varepsilon_0$, we obtain a steady shear flow with a shear rate of $2\varepsilon_0$ (Taylor 1934). However, a finite size drop would undergo different deformations in these two flow fields. For small deformation of a drop in a steady linear flow field, different approximations have been made to account for the effects of vorticity and rotation (Hakimi & Schowalter 1980), especially for deformation of high-viscosity-ratio drops. Rallison (1980, 1981, 1984) provided a unified version of

the small deformation theory. In §4 containing results, we compare drop deformation in a vortex with that in a shear.

2.2. Governing equations

The system is governed by the Navier–Stokes equation

$$\frac{\partial(\rho\mathbf{u})}{\partial t} + \nabla \cdot (\rho\mathbf{u}\mathbf{u}) = -\nabla p - \int_{\partial B} d\mathbf{x}_B \kappa \mathbf{n} \Gamma \delta(\mathbf{x} - \mathbf{x}_B) + \nabla \cdot [\mu\{\nabla\mathbf{u} + (\nabla\mathbf{u})^T\}], \quad (2.2)$$

in the entire domain Ω , consisting of the continuous phase Ω_c and the suspended drops Ω_d (figure 1*b*). p is the pressure, ρ the density and μ the viscosity of the fluid. The superscript T represents transpose. ∂B is the drop–fluid interface consisting of points \mathbf{x}_B , Γ is the constant interfacial tension, κ is the local curvature, \mathbf{n} is the outward normal to the interface, and $\delta(\mathbf{x} - \mathbf{x}_n)$ is the three-dimensional Dirac delta function. The stress due to interfacial tension is formally represented as a singular body force acting at the interface (Tryggvason *et al.* 1998), anticipating its numerical implementation using Front-tracking. It produces the jump in the normal stress across the drop interface. We do not consider Marangoni effects of interfacial tension variation due to non-uniform temperature or surfactant concentration. The evolution of interface $\mathbf{x}_B \in \partial B$ is coupled with the fluid velocity \mathbf{u} by

$$\frac{d\mathbf{x}_B}{dt} = \mathbf{u}(\mathbf{x}_B) = \int_{\Omega} d\mathbf{x} \delta(\mathbf{x} - \mathbf{x}_B) \mathbf{u}(\mathbf{x}). \quad (2.3)$$

The velocity field is incompressible:

$$\nabla \cdot \mathbf{u} = 0. \quad (2.4)$$

Material properties such as density or viscosity are assumed to be uniform within Ω_c and Ω_d and experience a jump across the interface ∂B . Such properties follow the motion of fluid, satisfying

$$\frac{D\phi}{Dt} = \frac{\partial\phi}{\partial t} + \mathbf{u} \cdot \nabla\phi = 0 \quad (2.5)$$

where $\phi(\mathbf{x})$ represents density $\rho(\mathbf{x})$ or viscosity $\mu(\mathbf{x})$. Although density difference is allowed in the current investigation, the buoyancy effects are not considered. Lastly, the velocity boundary condition is specified by equation (2.1), assuming the domain size is much larger than the size of the drop.

2.3. Non-dimensional parameters

Using initial drop radius R and inverse extensional rate $\dot{\epsilon}_0^{-1}$ as the length and time scales, respectively, we arrive at a number of non-dimensional parameters: Reynolds number $Re = \rho\dot{\epsilon}_0 R^2/\mu$, inverse capillary number (non-dimensional interfacial tension) $k = Ca^{-1} = \Gamma/(\mu\dot{\epsilon}_0 R)$, viscosity ratio $\lambda = \mu'/\mu$ and density ratio $\lambda_p = \rho'/\rho$. The prime denotes drop properties. For a vortex, the axis of stretching rotates at a fixed frequency, which corresponds to a fixed Strouhal number $St = \omega/\dot{\epsilon}_0 = 2$ (Sarkar & Schowalter 2001*a, b*).

3. Numerical implementation

The governing equations (2.2)–(2.5) are solved in a computational domain using a front-tracking finite difference method. The method is described in detail by Sarkar & Schowalter (2001*a*) and by Li & Sarkar (2005*a–d*). Here we provide only a brief

description. The method treats the multiple phases with different properties, separated by a sharp interface, as a single phase with the same set of equations in the entire domain. It therefore eliminates the need for satisfying velocity and stress continuity conditions at the moving interface. However, governing equation (2.2) is left with discontinuous viscosity and density, as well as singular forces due to interfacial tension. For computational purposes the discontinuity and the singular forces are replaced by ‘smoothed’ surrogates. They effectively replace the sharp interface by a diffuse one having the thickness of few (in this paper four) grid spacings. The resultant smoothed equations are solved in a regular Cartesian grid using an operator splitting/projection finite-difference method to obtain the velocity field. Unlike other similar methods such as VOF, level set or phase field, in this method the interface (front) is separately discretized by a mesh of triangular elements and tracked. The front evolves with the velocity interpolated at front points from the Cartesian grid using a smoothed version of equation (2.3). The new front position is used to determine the smoothed property fields and surface forces. In our simulation, to prevent the elements from being excessively distorted, an adaptive regridding scheme is implemented for the front. The topological changes of the front such as rupturing or merging can be handled by appropriately modifying the front mesh. Although two fronts close to each other such as happens during neck formation and breakup (less than four grid spacings) lead to error due to numerical smoothing near the interface, the qualitative features of topological change should still be captured in a spirit, similar to methods such as level set or volume of fluid (Renardy & Cristini 2001a). We also note that the breakup details might be critically affected by small-scale forces other than hydrodynamics, not considered in this simulation. In this paper, we do not investigate the detailed fragmentation after breakup.

4. Results

An initially spherical drop is placed at the centre of a cubic computational domain of size $L_d = 10R$. A fully developed linear flow (equation (2.1)) is assumed initially, and imposed at the boundary. Figure 2(a–f) shows the typical shape of a deforming drop in the linearized vortex at different time instants $t' = t\hat{\epsilon}_0$. The drop deforms from its initial spherical shape into an approximately ellipsoidal shape, and the axis of maximum elongation (dashed line) rotates counterclockwise following the axis of flow extension (solid line). The flow is strongly perturbed near the two ends of the drop. The velocity field inside the drop does not follow rigid-body rotation although from the shape of the drop it appears to. There exists a phase difference between the drop axis and the extension axis. For small capillary numbers, interfacial tension balances stretching due to the flow, giving rise to a dynamic steady state with a periodically rotating drop shape. For large capillary numbers, the capillary forces might not be sufficient, and the drop may experience breakup. Careful comparison of figures 2(b) and 2(f) shows that the drop is elongated after one flow period. The elongation eventually leads to breakup. The transient three-dimensional shape of the same drop approaching breakup is illustrated in figure 2(g–i). At the instant just before breakup ($t' = 4\pi$), the drop is highly elongated, with a narrow waist connecting two larger ends. It will eventually rupture at the waist. Note that at $t' = 4\pi$ the drop ends are approaching the simulation boundary; boundary effects are examined below (see §4.1). In the present study, the detailed process of fragmentation beyond this limit is not investigated.

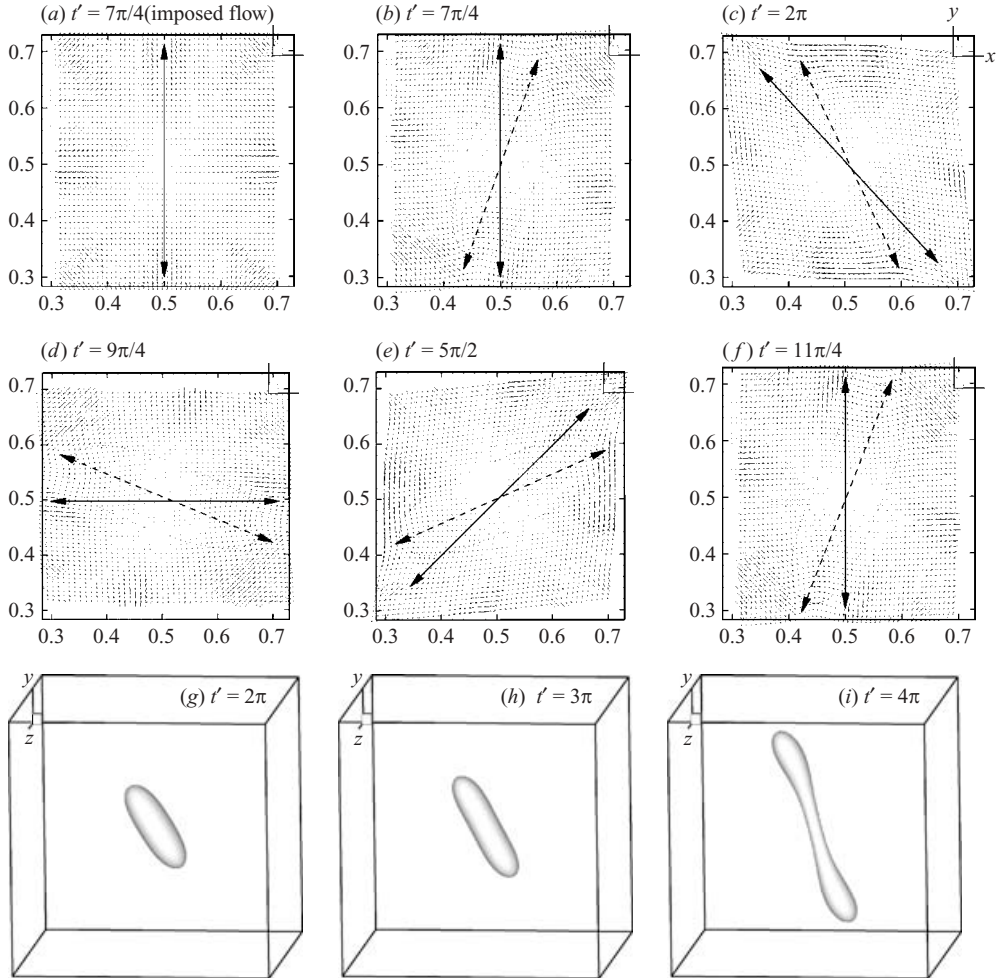


FIGURE 2. (a–f) Imposed flow and time-dependent drop behaviour in the (x, y) -plane through the centre of the drop; (g–i) The shape of a drop during breakup. $Re = 1.0$, $k = 10$, $\lambda = \lambda_\rho = 1.0$.

4.1. Convergence study

We performed a convergence study to investigate the ability of the present code to describe, in particular, the dynamic process of breakup. In figure 3(a), the time evolution of the deformation parameter D is plotted for the case of $Re = 1$, $\lambda = \lambda_\rho = 1$, $k = 50$, and a density-and-viscosity-matched drop. D is defined by Taylor (1932, 1934) as $(L - l)/(L + l)$, where L and l are the maximum and minimum surface-to-centre distances, respectively. Following an initial transient overshoot, D reaches a steady value with slight numerical oscillations. As the discretization is increased from $65 \times 65 \times 65$ to $161 \times 161 \times 161$, the steady deformation D_s converges to a value around 0.055. The numerical oscillations also reduce on refining grid levels. We choose $113 \times 113 \times 113$ for our simulation. Although a slight deviation of D from the converged value exists at this level, the actual drop shape matches well with that at $161 \times 161 \times 161$, as displayed in the inset. The quadratic rate of convergence of D_s is also shown in the inset.

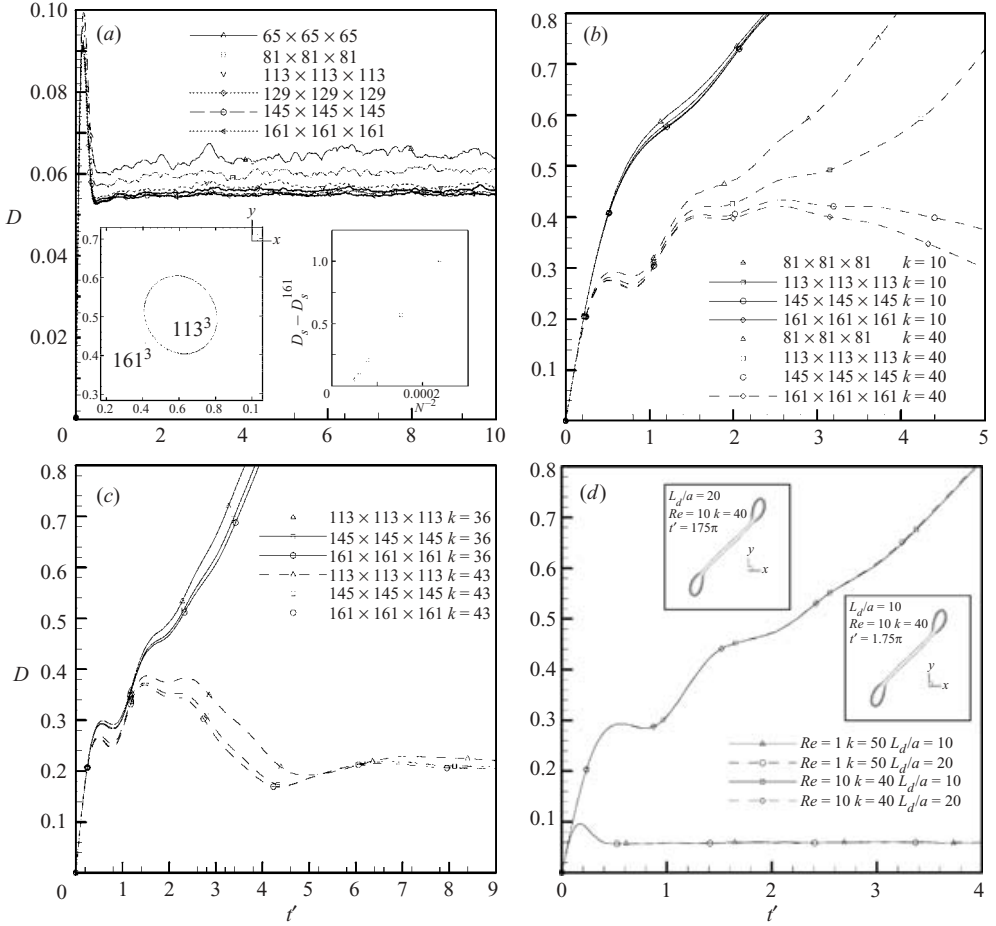


FIGURE 3. Convergence of deformation D with varying discretizations for (a) $Re = 1.0, k = 50, \lambda = \lambda_\rho = 1$ (bounded deformation), (b) $Re = 10.0, \lambda = \lambda_\rho = 1, k = 10$ (breakup) and $k = 40$; and with varying domain size in (d) for $\lambda = \lambda_\rho = 1$. Near critical breakup condition, D shows divergence as in plot (b) for $Re = 10.0, \lambda = \lambda_\rho = 1, k = 40$. In (c) the convergence of D slightly away from the critical condition is shown.

In figure 3(b), the deformation D at $Re = 10, \lambda = \lambda_\rho = 1, k = 10, k = 40$ is plotted for various discretizations. For $k = 10$, the drop experiences unbounded growth indicating breakup. We observe convergence of D similar to figure 3(a). For $k = 40$, at $145 \times 145 \times 145$ and $161 \times 161 \times 161$, a bounded deformation is observed in contrast to unbounded growth at coarser levels. The results indicate that $k \sim 40$ corresponds to a critical condition for breakup. In figure 3(c), just below ($k = 36$) and above ($k = 43$) the critical condition, we obtain an unbounded and a bounded deformation respectively, and the simulation converges with grid refinement in both cases. This implies that although it becomes difficult to obtain grid convergence at the critical limit, away from it the simulation becomes insensitive to discretization, and critical breakup conditions can be estimated within a certain error-bound using the present simulation methodology.

In figure 3(d), the wall effects are checked by doubling the size of the domain L_d/a for the same cases investigated in figure 3(a, b). Neither bounded nor unbounded

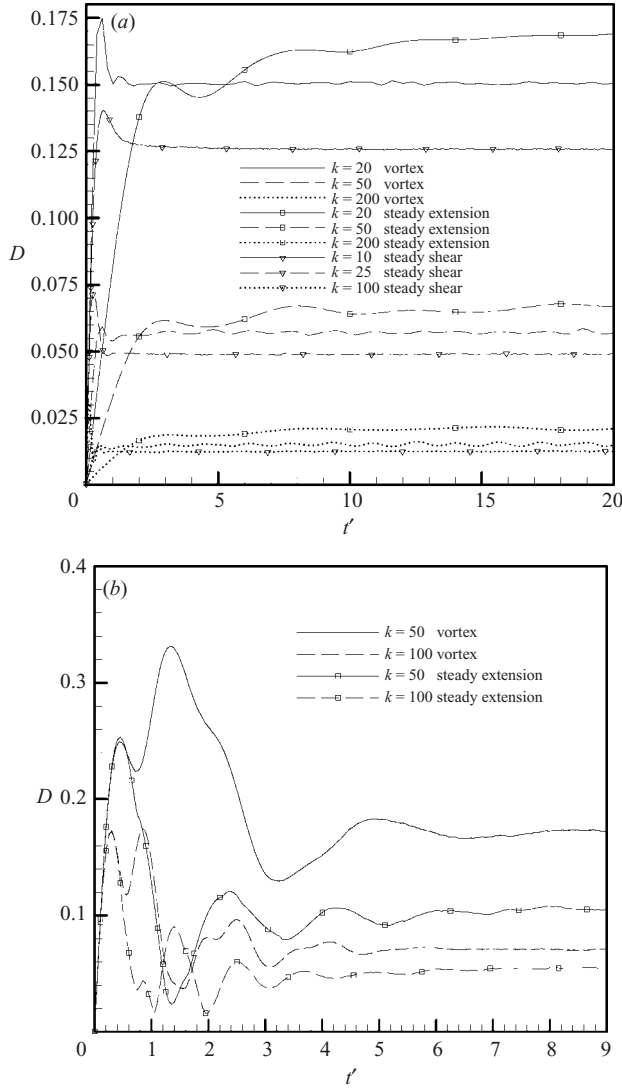


FIGURE 4. D vs. t' with varying interfacial tension parameter k for $\lambda = \lambda_\rho = 1$: (a) $Re = 1$, (b) $Re = 10$.

deformations are affected by the increase of L_d . Even the shape of a stretched drop at the same time instant does not display much difference with different domain sizes. Very slight deviation appears only for highly elongated drop with large deformation ($D > 0.6$) when the drop starts being affected by the existence of boundary.

4.2. Drop deformation: effects of the rotation of the extension axis

We first consider the case of a viscosity-and-density-matched drop where the drop is manifested solely by the presence of interfacial tension. As was mentioned in § 2.1, the velocity gradient (rotating extension) of a vortex transforms into a steady shear under a rotation of coordinate axes. In figure 4(a), we plot the deformation D vs. t' with varying interfacial tension parameter k at $Re = 1$, $\lambda = \lambda_\rho = 1$ in a steady extension, a vortex and a steady shear. Note that for shear the values of k have been taken to be

half that in the other cases, for a velocity gradient in a vortex is equivalent under the coordinate transformation to a shear with twice the amplitude. As already mentioned, in a vortex after a short transient the drop achieves an approximately ellipsoidal shape with its maximum axis rotating with the frequency of the imposed flow. This results in an unvarying value of D in the long-time limit. As expected, the increase of interfacial tension k leads to decreased deformation D . The long-time deformation reaches a larger value in steady extensions for all k considered. Rotation inhibits deformation as the drop does not have sufficient time to stretch before the maximum stretching moves to different point on the drop boundary. A similar inhibition of deformation due to the rotational component of the velocity gradient has been noted in Stokes flow steady shear (Taylor 1934; Bentley & Leal 1986) for high-viscosity-ratio drops. However, the deformation in a shear flow at finite inertia is less than that in the vortex. Rallison (1981) showed that for sufficiently small deformation and for imposed velocity gradient having the same orders of magnitudes of stretching and rotation the deformation is determined only by the stretching part, thereby predicting the same deformation in a shear and a vortex. However, at finite Reynolds numbers and for large deformations, extension, shear and rotating extension (in a vortex) flows are all different in their effects on the drop, as is seen in figure 4(a).

In figure 4(b), we increase the Reynolds number to $Re = 10$. As reported by Ramaswamy & Leal (1997) and Li *et al.* (2000), inertia promotes deformation. Indeed at large Reynolds number, as mentioned before, the drop dynamics is determined by the balance between capillary and the inertial forces. At $k = 50$, the steady deformation D_s increases from $D_s \approx 0.05$ for $Re = 1$ (figure 4a) to $D_s \approx 0.17$ for $Re = 10$. Increased inertia also leads to significant oscillations during the initial transient. As k is doubled from $k = 50$ to 100, the period of such oscillations T (the difference of t' between two maxima) decreases from around 0.9 to 0.6. This can be explained by the a second-order ODE model described in the Appendix. The drop in a vortex is modelled as a forced-damped mass-spring system (Sarkar & Schowalter 2001a). The governing ODE predicts a non-dimensional natural frequency of free oscillation $\hat{S}t_n = \sqrt{2\hat{k}/[(1 + \hat{\lambda}_\rho)\hat{R}e]}$. For the present case, $\hat{T}_{\hat{k}=50}/\hat{T}_{\hat{k}=100} = \hat{f}_{\hat{k}=100}/\hat{f}_{\hat{k}=50} = \sqrt{2}$, which matches the simulated results $T_{k=50}/T_{k=100} \approx 0.9/0.6 \approx \sqrt{2}$. Oscillations during transients were also found in a finite-inertia computation of a drop in steady shear by Renardy & Cristini (2001a). Corresponding to figure 4(a), we plot the deformation D for drops in simple extensional flow in figure 4(b). In contrast to figure 4(a) for $Re = 1$, the simple extensional flow at $Re = 10$ leads to smaller deformation than the vortex flow. The imposed rotating flow induces a pressure field at finite inertia due to the balance of $\rho \partial \mathbf{u} / \partial t \sim \nabla p$ in the Navier-Stokes equations. The enhanced deformation is caused by this rotation-induced pressure field which becomes dominant at the higher Reynolds number. This effect can be explained by the ODE given in the Appendix. Note that $|X|$ from (A 6) mimics deformation. The enhancement in deformation is due to the dominance of the second term of order $\sim \hat{R}e^2 \hat{S}t^2$ in the denominator that results from the pressure term in the governing equation (A 1). We conclude that the rotation of the extension axis inhibits drop deformation at low Re but promotes it at high Re .

To investigate further the effects of Reynolds number, in figure 5, the steady-state drop shape together with the flow field in the (x, y) -plane through the centre of the drop at the same time instant is displayed. The cases of vortex flow and simple extensional flow are compared at different k and Re . At $k = 100$ and $Re = 1$ (figure 5a), similar fields are observed for both flows, with slightly stronger eddies and smaller deformation for the vortex (also see figure 4a). In figure 5(b), with increase of inertia

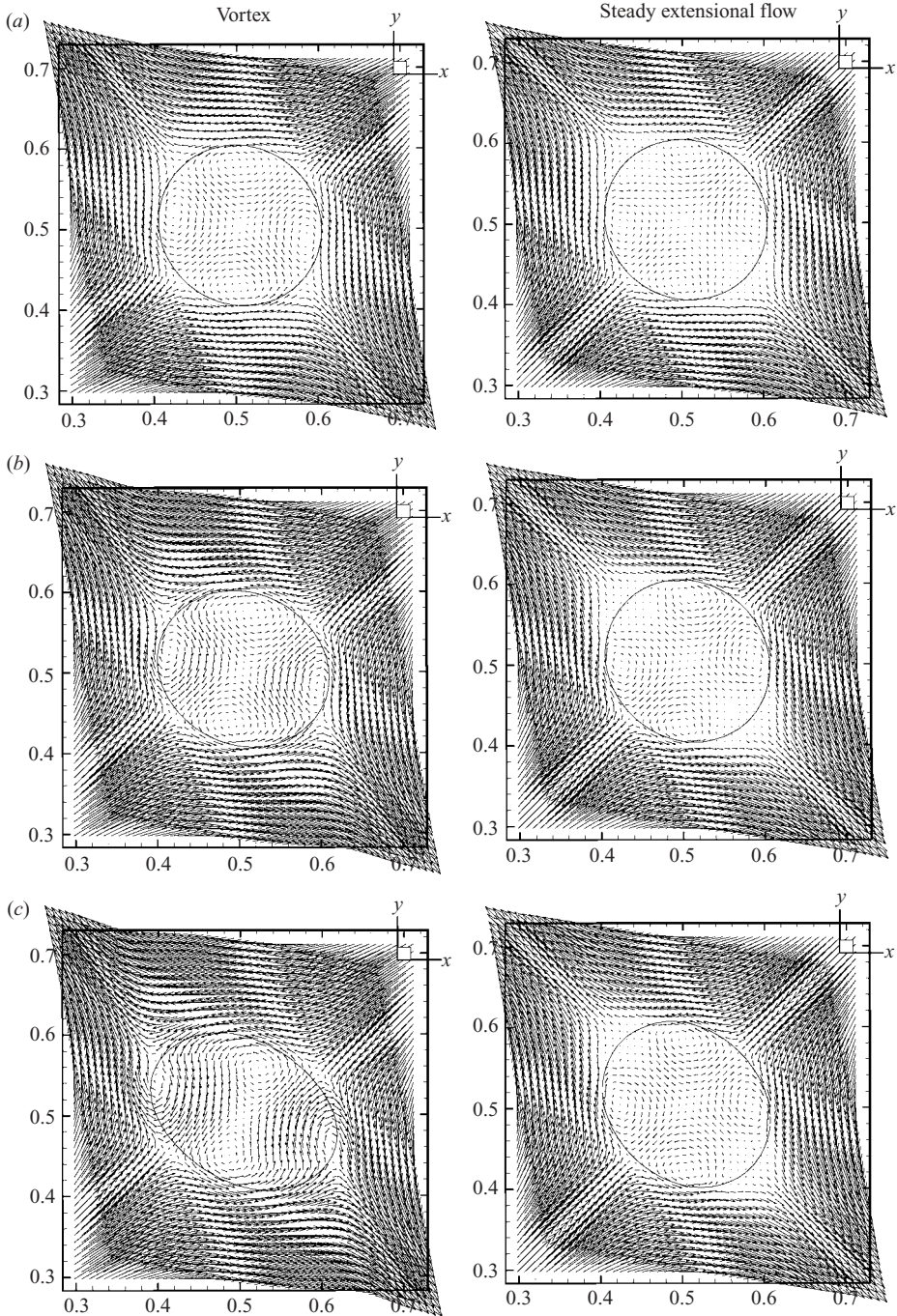


FIGURE 5. Comparison of flow and drop shape in the (x, y) -plane through the centre of the drop, for vortex and steady extensional flow in steady state, $\lambda = \lambda_\rho = 1$: (a) $Re = 1, k = 100$; (b) $Re = 10, k = 100$; (c) $Re = 10, k = 50$.

to $Re = 10$, the flow symmetry about the drop axis is broken in vortex flow (see the phase difference), while no significant change of flow structure appears in simple extensional flow. For vortex flow at $k = 100$ and $Re = 10$ (figure 5b), two stronger

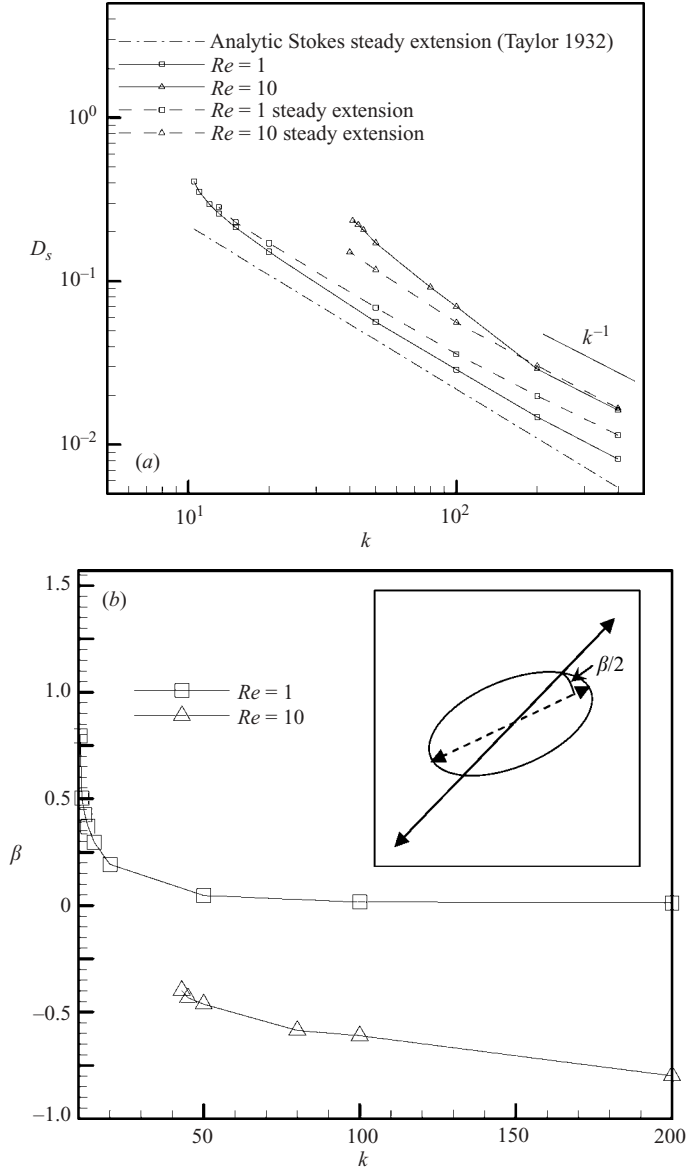


FIGURE 6. (a) Steady-state deformation D_s and (b) phase lag β vs. k ; $\lambda = \lambda_\rho = 1$. Inset of (b) shows the definition of phase lag β .

eddies emerge near the two ends due to the counterclockwise rotation. At high inertia ($Re = 10$), an additional centrifugal force in the vortex is acting on the deformed (non-spherical) drop to push interior fluid towards the two ends, generating a large dynamic pressure there. For lower interfacial tension parameter $k = 50$ and $Re = 10$ (figure 5c), the ratio of the centrifugal force to interfacial tension is larger, leading to increased deformation and prominent asymmetry in the vortex.

In figure 6(a), the long-time deformation D_s vs. k is plotted at different Re for both vortex and steady extension flows. D_s decreases monotonically with increasing k . At large k , a $D_s \sim k^{-1} = Ca$ scaling is observed. Note that such a scaling holds in

both Stokes flow (Taylor's analytical result is shown) and flows with inertia (Sarkar & Schowalter 2001*a, b*; Renardy & Cristini 2001*a*). It is predicted by the ODE model in the Appendix as well, $|X| \sim \hat{k}^{-1}$ as $\hat{k} \rightarrow \infty$. The onset of asymptotic scaling is delayed for the higher Reynolds number case. Similarly to figure 4, the vortex (at $k = 50$) induces smaller deformation at low inertia ($Re = 1$) and larger deformation at higher inertia ($Re = 10$) compared to steady extension. As the interfacial tension parameter k increases, the inhibitive effects due to axis rotation gradually dominate centrifugal effects, and even at the higher Reynolds number of $Re = 10$, the vortex inhibits deformation, roughly at higher than $k = 400$.

The drop axis does not rotate in phase with the flow axis, as shown in figure 2. In figure 6(*b*), the variation of phase lag β with k is plotted in steady state. β is defined in the inset as twice the angle between the axis of stretching and the drop axis (one period for the drop corresponds to half a period for the flow). β decreases with increasing k , reaching a constant asymptotically for large k . Note that for $Re = 1$, β is positive, while for $Re = 10$, β becomes negative, indicating that the phase of the drop response is ahead of the flow. As we mentioned before, rotation induces a pressure field for finite inertia. The rotation-induced pressure field is out of phase with the imposed velocity. The phase response of the drop is governed by both the viscous force and the induced dynamic pressure. The behaviour can be explained by the ODE model (see the Appendix). The phase lag is mimicked by the model parameter $\hat{\beta}$; the negative value of β is due to the negative second term in equation (A 7) which is a result of the dynamic pressure. It eventually dominates the first term as \hat{k} increases at finite Re . Li & Sarkar (2005*a*) observed similar behaviour for the deformation phase for a drop in an oscillating extensional flow. The phase between the imposed flow and the drop response plays an important role in the overall rheological response of an emulsion of drops. The phase between the imposed strain and the effective stress of the emulsion determines the viscous and viscoelastic part of the effective stress (Li & Sarkar 2005*b, c, d*).

4.3. Inertia-driven breakup and critical behaviour

Fluid inertia promotes drop deformation. Continuously increasing Re eventually leads to drop breakup. In figure 7(*a*), at $k = 10$, $\lambda = \lambda_\rho = 1$, an increase of Re induces a rapid increase of deformation D . For $Re > 0.3$, the drop does not reach a bounded shape; the interfacial tension fails to balance the dynamic pressure leading to inertia-driven breakup. In figure 7(*b*), the drop shapes at the same instant before breakup are plotted. For breakup at low inertia ($Re = 1.0$, left), the drop is significantly stretched to a slender shape ($L/l \gg 1$) before rupture due to capillary instability. However, in vortex flow at higher inertia ($Re = 10.0$ right), centrifugal forces push the interior fluid towards the ends. The perturbation flow fields due to the drop are shown as well. Strong perturbation occurs near the end regions with large curvature, where the interfacial tension induces the largest stresses.

For a fixed interfacial tension parameter k , there exists a critical Re for breakup, and correspondingly for a fixed Re , there is a critical k . In figure 8, we plot critical capillary number $Ca_{cr} = k_{cr}^{-1}$ as a function of Re . The critical values are determined by decreasing Ca (or increasing k). The Ca at which the drop starts to attain bounded deformation is taken as the critical value. Since deformation D displays divergence near critical conditions (figure 3*b*), the critical Ca obtained using the present discretization ($113 \times 113 \times 113$) is in fact a lower bound, i.e. below this value the physical solution of D must be bounded. The upper bound of the critical value (shown in the plot for some Re) is determined as the Ca at which the drop starts to

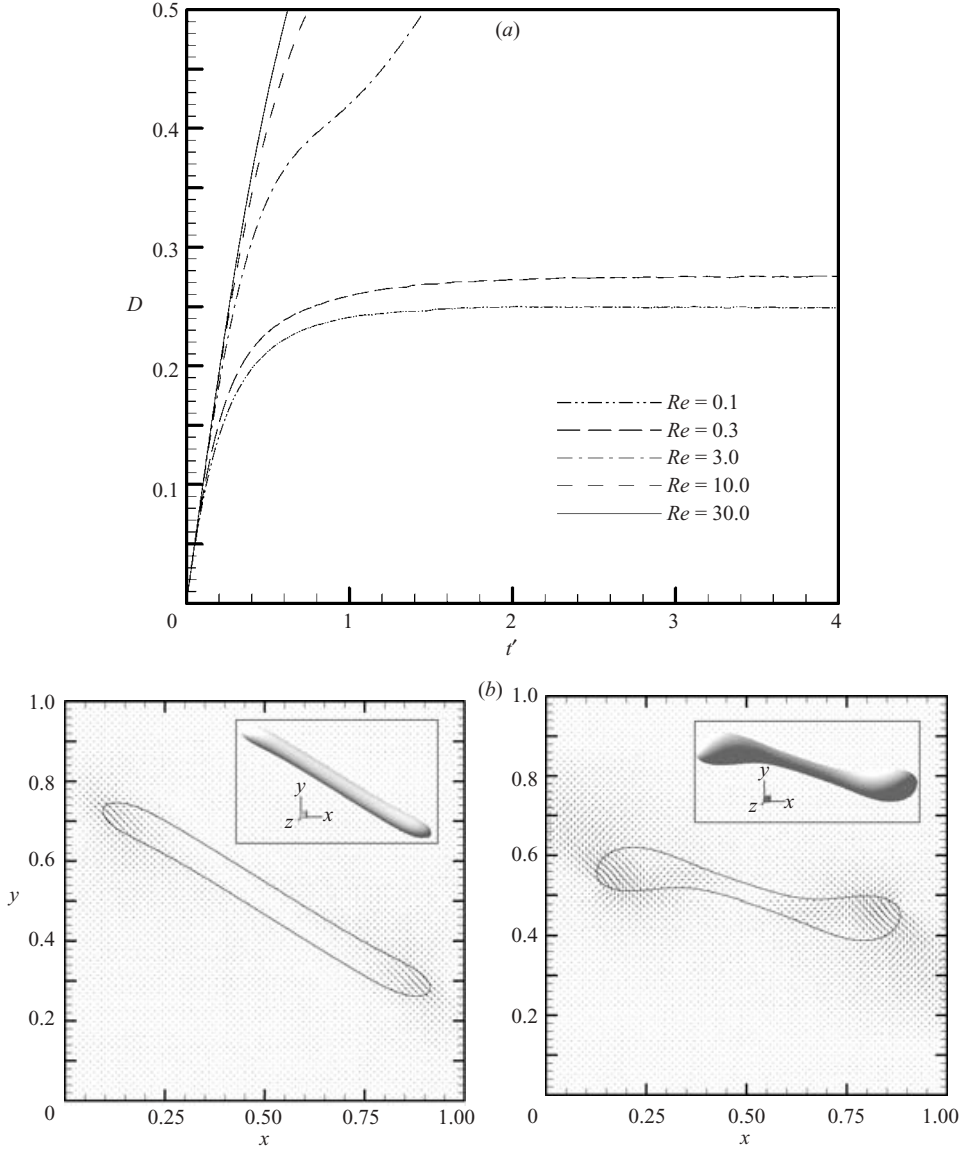


FIGURE 7. (a) D vs. t' for varying Re at $k = 10$, $\lambda = \lambda_\rho = 1$. (b) The drop shape together with perturbation flows just before breakup for: $t' = 4\pi$, $Re = 1$, $k = 5$ (left) and $t' = 4\pi$, $Re = 10$, $k = 35$ (right).

show converged unbounded deformation for all discretizations as Ca is increased. As seen in figure 8, Ca_{cr} decreases with increasing Re . At low inertia ($Re = 0.1$), we find $Ca_{cr} \approx 0.2$ in vortex flow in comparison with Leal's experimental value $Ca_{cr} \approx 0.13$ in steady extension (These experiments were performed at a much smaller Reynolds number; Bentley & Leal 1986.) Note that the experiments were performed starting from a rest state and increasing the velocity slowly to its final value, so that the drop goes through equilibrium states at every intermediate stage. As a result, they noted that the value of the critical capillary number they obtained is really a physical upper limit over all possible values that may occur for different flow histories. The higher

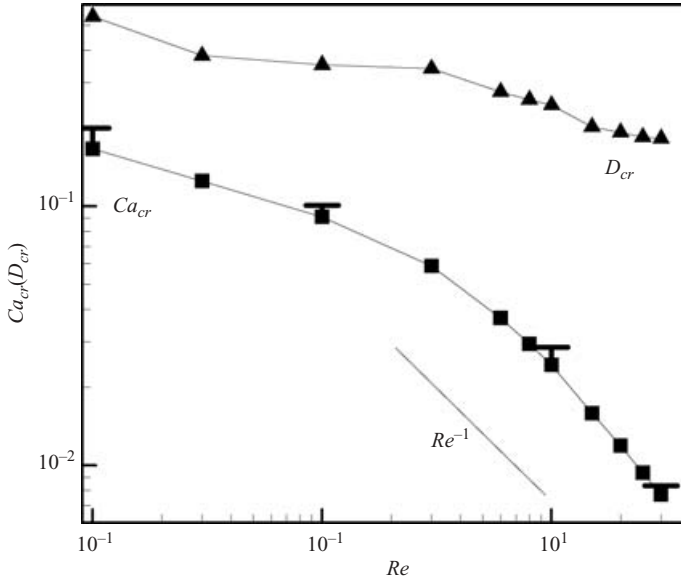


FIGURE 8. The critical capillary number Ca_{cr} and critical steady deformation D_{cr} vs. Re .

values of Ca_{cr} obtained here are due to reduced stretching in the rotating vortex flow. For large inertia ($Re > 20$), figure 8 shows that Ca_{cr} reaches an inviscid limit. The Weber number $We_{cr} = ReCa_{cr}$, which is independent of viscosity, determines the critical behaviour, giving rise to $Ca_{cr} \sim Re^{-1}$ scaling for $Re > 20$. We found the critical Weber number in this case to be $We_{cr} \approx 0.23$. Similar scaling has been reported in simple shear and extensional flow (Ramaswamy & Leal 1997; Renardy & Cristini 2001a). The critical long-time deformation D_{cr} (also shown in figure 8 on the same ordinate axis) correspondingly shows a decrease with increasing Re , and finally reaches an asymptotic value of around 0.2 as $Re \rightarrow \infty$.

4.4. Behaviour with varying viscosity ratio

At a fixed $Re = 1$, we investigate the effects of viscosity ratio by increasing λ from 0.01 to 10.0. The evolution of D with different viscosity ratios is plotted in figure 9(a). For smaller λ , its increase, e.g. from 0.01 to 0.3, leads to increased deformation from 0.3 to 0.35. At $\lambda = 3.0$, the drop shape undergoes continuous stretching, leading to fragmentation. On further increase of λ from 3.0 to 10.0, however, a steady bounded drop shape is attained. The phenomena can be explained as due to the increased damping at higher drop viscosity (Sarkar & Schowalter 2001b), which is also found in Stokes shear flow (Bentley & Leal 1986).

Figure 9(b) shows drop shape and flow field at the same time instant for two different λ values, keeping other parameters fixed. With increasing λ , the phase-lag between the maximum axis of the drop and that of the extension increases. At $\lambda = 0.1$, four strong eddies form asymmetrically inside the drop. Note that the shape of the drop in vortex flow at $\lambda = 0.1$ appears nearly ellipsoidal in contrast to the spindle shape with two sharp tips in steady extension flow (Bentley & Leal 1986). The velocity at the tips is non-zero, in accordance with the rotating kinematics of vortex flow. At higher viscosity ratio $\lambda = 10.0$, only a single weak eddy is observed inside the drop with the fluid approaching rigid body rotation due to the large drop viscosity. A

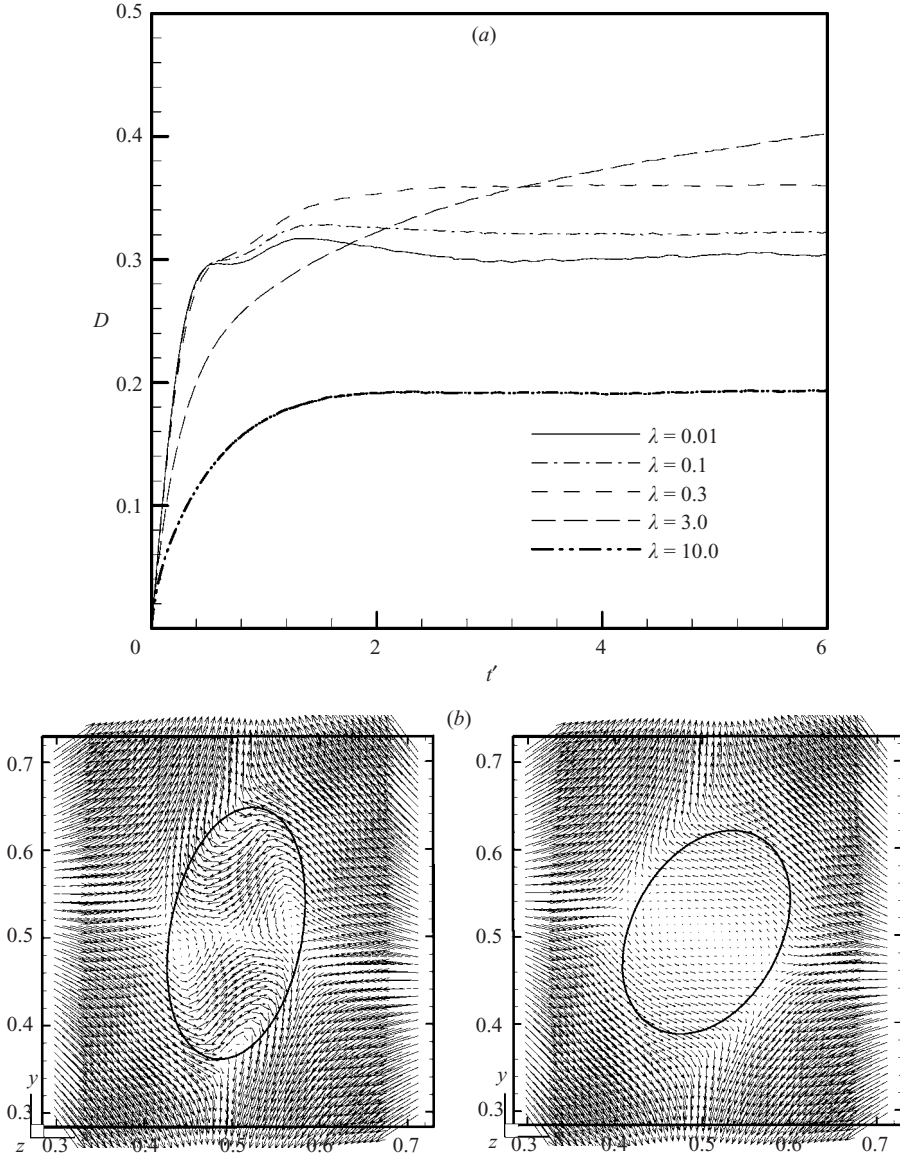


FIGURE 9. (a) D vs. t' and (b) detailed flow and drop shapes at $Re = 1$, $k = 10$, $\lambda_p = 1$ and different viscosity ratio $\lambda = 0.1$ (left), $\lambda = 10.0$ (right).

similar structure appears for high-viscosity drops in simple shear (Stone 1994). At high viscosity ratio, the drop behaviour in vortex flow resembles that in shear instead of extension flow, due to the rotation of the stretching axis.

In figure 10, Ca_{cr} is plotted as a function of λ . Similarly to figure 8, we determined the numerical lower bound and upper bound of the critical value. The vortex flow results are compared to two steady linear flow experiments by Bentley & Leal (1986) – one is an extensional flow that does not have any rotational or antisymmetric component in the velocity gradient (characterized by $\alpha = 1$, note that $\alpha = 0$ corresponds to simple shear) and the other one with a rotational component ($\alpha = 0.2$). Ca_{cr} varies non-monotonically with λ , slightly decreasing with λ at low λ but increasing at high λ

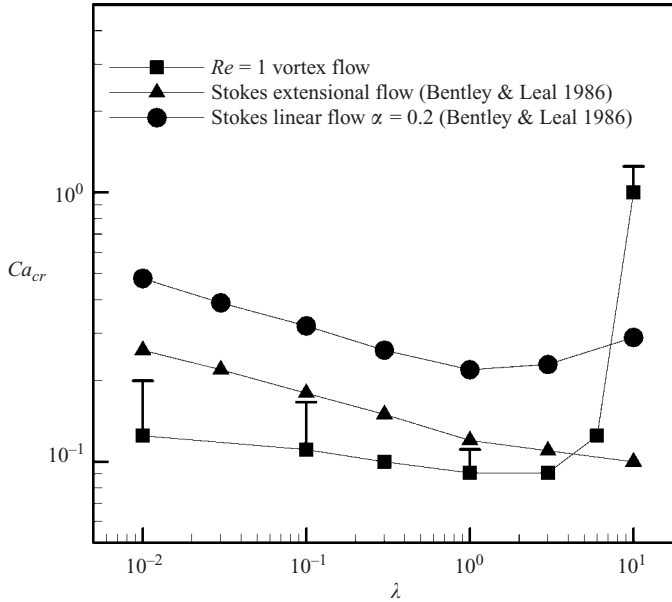


FIGURE 10. Critical capillary number Ca_{cr} vs. λ ; $\lambda_\rho = 1$. The simulation data for vortex flow at $Re = 1$ are compared with experimental results in linear Stokes flow.

for the vortex and the linear flow with rotation. At $\lambda = 10$, a very large flow strength ($Ca > 1.0$) is required to burst the drop. As seen in figure 9(b), high viscosity ratio leads to significant damping due to fluid rotation inside the drop, reducing the net stretching force and making the breakup difficult.

4.5. Density ratio variation: resonance breakup

At density ratio different from unity, the drop experiences a centrifugal force leading to a radial drift in the drop across circular streamlines associated with the vortex flow. The Stokes number signifying the particle response time relative to the characteristic time of the flow determines the drift. Here we have not considered this radial motion. In figure 11(a), we plot D at $Re = 1$, $k = 10$, $\lambda = 1$ but with varying density ratio λ_ρ . At $\lambda_\rho = 0.1$ and 0.3, the deformation attains a bounded value. At $\lambda_\rho = 3$, the deformation is enhanced leading to unbounded growth. However, as λ_ρ is further increased to 10, the deformation appears to remain bounded after $t' = 7$. At $\lambda_\rho = 30$, the drop attains a bounded steady shape with lower deformation in the long time limit although it shows long transients with significant oscillation. In figure 11(b), D is plotted at different interfacial tension parameter k but fixed $\lambda_\rho = 10$. The deformation in the initial part decreases with increasing interfacial tension. However, for $k = 2, 5$ and 10, D changes characteristics and they cross each other around $t' \approx 4$. The long-time deformation D_s increases with increase in k . At $k = 16$, the drop cannot attain an equilibrium shape. As k is further increased to 20, however, a bounded deformation is achieved. In figure 11(a) and 11(b) the long-time deformation varies non-monotonically with increasing viscosity ratio and interfacial tension parameter respectively. In figure 11(c), at $\lambda_\rho = 10$, but at an increased drop viscosity $\lambda = 10$, the oscillations of D during transients are damped, and a monotonic decrease of the long-time deformation with increasing k is observed.

Figure 11(d) summarizes the long-time deformation by plotting D_s vs. k for different λ_ρ and λ . For the range of k where the drop ruptures, a long-time steady deformation

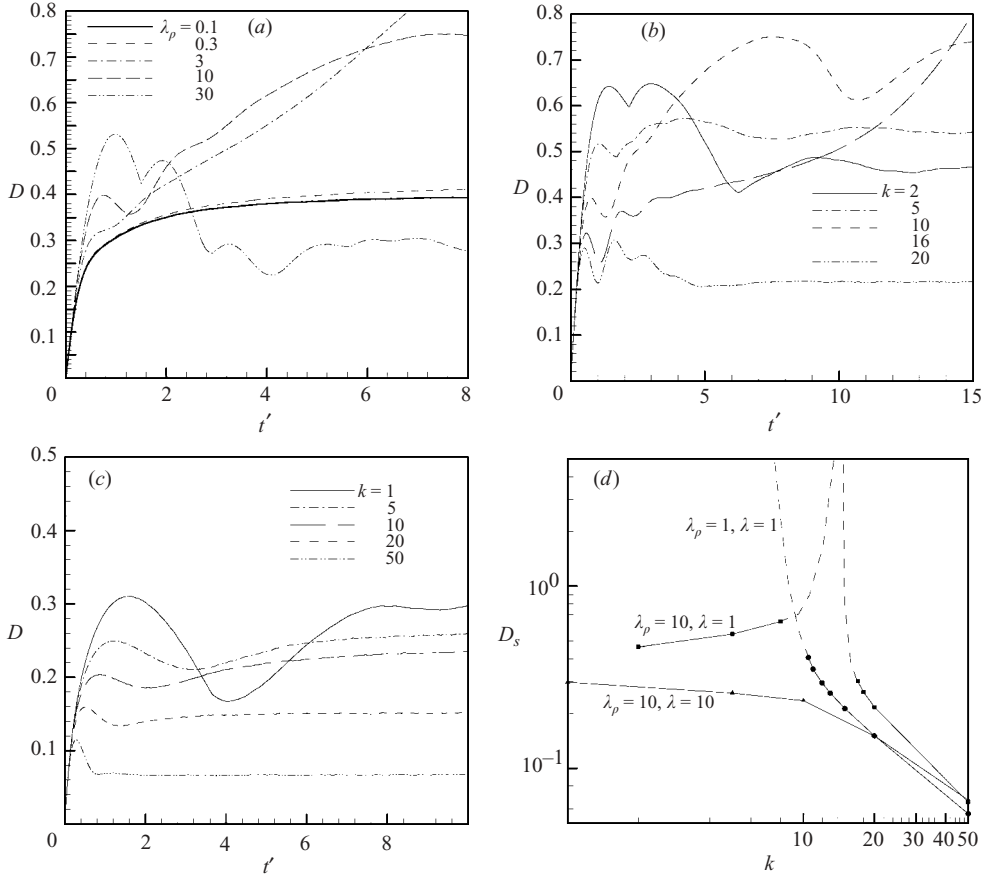


FIGURE 11. D vs. t' with variation of (a) density ratio λ_ρ , $Re = 1, k = 10, \lambda = 1$; (b) k , $Re = 1, \lambda = 1.0, \lambda_\rho = 10$; (c) k , $Re = 1, \lambda = 10.0, \lambda_\rho = 10$. (d) Steady-state deformation D_s vs. k at $Re = 1$ with variation of λ_ρ and λ .

does not exist; dashed curves are used to illustrate the tendency. We also include the curve for $\lambda = 1, \lambda_\rho = 1$ along with $\lambda = \lambda_\rho = 10$ for comparison. The characteristics of the $\lambda = 1, \lambda_\rho = 10$ case are significantly different from the other two cases. The non-monotonic variation and the large deformation/breakup at intermediate k values can be explained by resonance. The resonance phenomenon was suggested and explored in detail by Sarkar & Schowalter (2001a) for two-dimensional drop deformation in rotating and oscillating extensional flows. They also provided a perturbative small deformation analysis (Sarkar & Schowalter 2001b) that matched very well with the numerical simulation. Furthermore, they developed a second-order (ODE) model for a qualitative description of the drop deformation as a forced-damped mass-spring system (provided in the Appendix). Here the surface tension acts as a spring, viscosity as a damping element and imposed periodic flow as forcing. As predicted by the ODE model, the drop has a natural frequency, which depends on the variation of interfacial tension parameter k , density ratio λ_ρ and Reynolds number Re . The model non-dimensional natural frequency is $\hat{S}t_n = \sqrt{2\hat{k}/[(1 + \hat{\lambda}_\rho)\hat{Re}]}$ (see the Appendix). When the natural frequency matches the frequency of rotation in a vortex, the drop undergoes resonance leading to a large deformation and possible rupture. With a decrease in interfacial tension parameter k or increase in λ_ρ , the natural

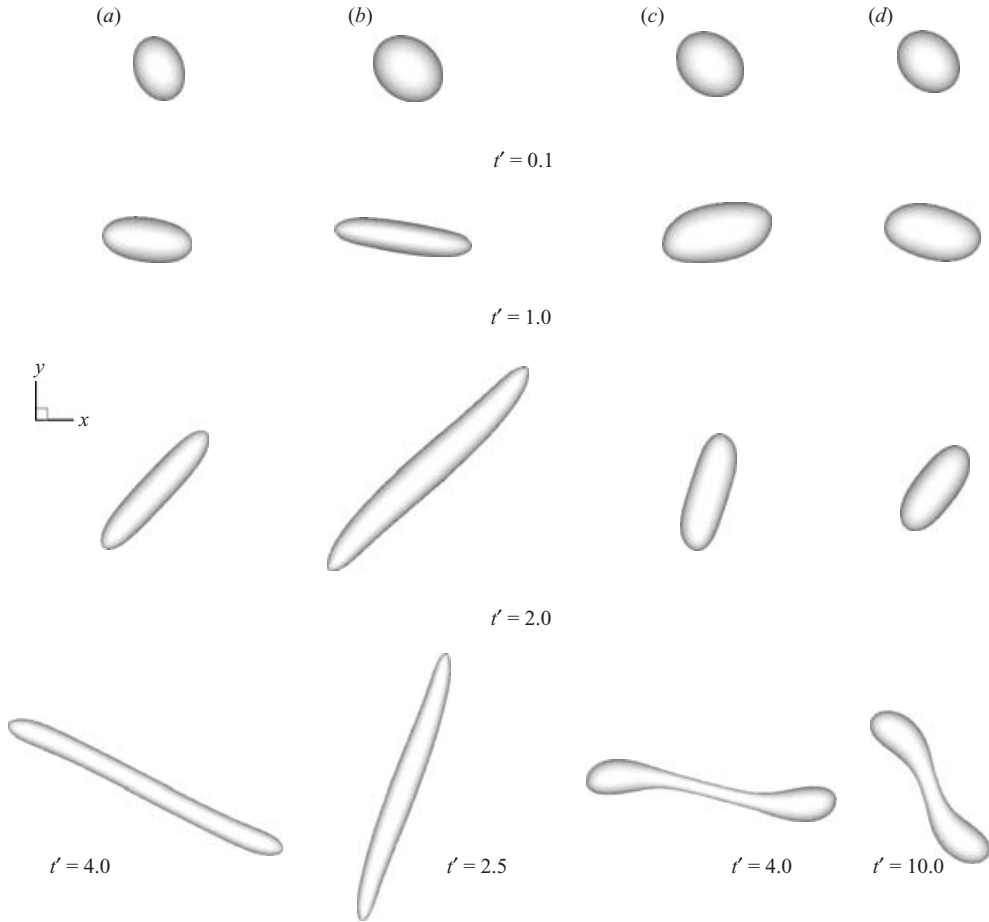


FIGURE 12. History of drop breakup: (a) $Re = 1, k = 5, \lambda = \lambda_\rho = 1$; (b) $Re = 10, k = 5, \lambda = \lambda_\rho = 1$; (c) $Re = 10, k = 35, \lambda = \lambda_\rho = 1$; (d) at resonance $Re = 1, k = 15, \lambda = 1, \lambda_\rho = 10$.

frequency of the drop decreases. For the vortex flow the forcing frequency is very low ($St = 2$). Correspondingly, at resonance, for density-matched drops, k is too low for the interfacial tension forces to balance the stretching due to the flow. The drop breaks, and the small deformation theory of resonance loses its validity (Sarkar & Schowalter 2001*a, b*). That explains why the ascending part of the D_s vs. k curve is not observed for drops with $\lambda_\rho = \lambda = 1$, as was also the case in two dimensions (Sarkar & Schowalter 2001*a, b*). However, as the density ratio is increased to $\lambda_\rho = 10$, resonance shifts towards larger k in figure 11(*d*), and the drop attains a bounded shape for smaller k to the left of resonance. In the vicinity of resonance the deformation becomes large leading to breakup. Note that the non-monotonic variation with rupture at $\lambda_\rho = 3$ in figure 11(*a*) is also due to resonance. We conclude that high-density drop can experience a different breakup route through resonance in a vortex. Vortex flows can act as a model of turbulent eddies. In such flows, resonance may lead to breakup at relatively low strain rate, if the size and density are appropriate to achieve resonance. Kang & Leal (1990) found a similar resonance-induced breakup of bubbles in a subcritical time-periodic straining flow with optimized frequency. Risso & Fabre (1998) also suggested similar resonance breakup of bubbles in turbulent flows. Finally in figure 12, we present the evolution of the drop shapes when they break

under different conditions. At low Reynolds numbers, breakup takes place for low values of k when viscous forces overcome the capillary force. At higher Reynolds number breakup shapes are different for small and large values of surface tension. Unlike the smaller value of $k=5$, at $k=35$ the drop takes a dumbbell shape. For breakup initiated by resonance, the drop shape is similar to the high Reynolds number case.

5. Summary

In this paper, the deformation and breakup of a viscous drop in an important time-dependent flow – potential vortex – has been computationally investigated. The flow can act as a model for eddies in turbulent flows, and can be set up in a laboratory for determining rheological responses. A drop in such a flow experiences extension with a rotating axis of extension. This flow is related to a steady shear flow by a rotation of the reference frame. The effects of these two flows on the deformation of a drop, although having some resemblance, e.g. rotation inhibits deformation at small Reynolds number, are shown to be quite different. The drop has a very different flow history in these two flows.

For density-and-viscosity-matched drops, the deformation is inhibited in a vortex flow compared to that in a steady extension flow at low Reynolds numbers. At high Reynolds number however, deformation is promoted due to an additional rotation-induced pressure force. Correspondingly, drop breakup is found to be governed by different mechanisms at different Re which gives rise to different drop shapes. At lower Reynolds number, the drop lags the rotating extension, similarly to what happens in a steady shear Stokes flow. However, at higher Reynolds number the phase angle becomes negative due to the flow-induced pressure field, and the drop leads the extension axis. Like simple extension in Stokes flow, an increase of drop viscosity leads to larger viscous forces and larger deformation when viscosity ratio is small, but for drops with high viscosity, the axis of rotation induces significant rotational flow inside the drop, reducing drop deformation. We found critical a capillary number for drop breakup in a vortex for varying Reynolds number and viscosity ratio, and compared it with other flows. We found that the critical capillary number scales with the inverse of the Reynolds number at high Reynolds numbers, indicating that the inertial breakup is determined by the Weber number ($We_{cr} \approx 0.23$). With varying viscosity ratio, the critical capillary number reaches a minimum at a particular value of the viscosity ratio, a phenomenon observed also in steady shear.

In a two-dimensional simulation (Sarkar & Schowalter 2001*a, b*), we found that a drop in time-periodic flows can experience resonance-induced enhancement of deformation when the natural oscillation frequency of the drop matches the forcing frequency. As a result, the deformation shows non-monotonic variation with interfacial tension parameter and Strouhal number of the forcing flow. However, for a vortex, the Strouhal number ($=2$) is too low to induce resonance for the density-and-viscosity-matched drop that was considered by Sarkar & Schowalter (2001*a*). In the current investigation, we find that a drop with density larger than that of the surrounding fluid can experience larger deformation with possible breakup. This provides an alternative mechanism for size-selective breakup of drops with a particular density in turbulent eddies.

The authors acknowledge one of the reviewers for his comments regarding the critical shape at breakup and radial drift. K.S. acknowledges support from the

University of Delaware College of Engineering and the Department of Mechanical Engineering.

Appendix. A simple mass–spring–dashpot model

The dynamics of drop deformation in a vortex can be qualitatively described by a simple ODE model introduced by Sarkar & Schowalter (2001a). A drop subjected to vortex flow can be modelled as a mass–spring–dashpot system with mass $(1 + \hat{\lambda}_\rho)\hat{\rho}\hat{R}^3/2$, damping $(1 + \hat{\lambda})\hat{\mu}/2$ and spring $\hat{\Gamma}$ (interfacial tension). \hat{R} is the drop radius. The hat is used to differentiate the model variables from their real counterparts. Forced by the vortex flow represented as $G_0g(t)$ (G_0 is the velocity magnitude, $g(t)$ indicates time-periodicity), drop deformation is modelled by a second-order ODE:

$$\frac{1 + \hat{\lambda}_\rho}{2}\hat{\rho}\hat{R}^3\ddot{X} + \frac{1 + \hat{\lambda}}{2}\hat{\mu}\hat{R}\dot{X} + \hat{\Gamma}X = \frac{1 + \hat{\lambda}}{2}\hat{\mu}\hat{R}G_0g(t) + \frac{1 + \hat{\lambda}_\rho}{2}\hat{\rho}\hat{R}^3G_0\dot{g}(t). \quad (\text{A } 1)$$

The initial condition is

$$\dot{X}(0) = G_0g(0), \quad X(0) = 0. \quad (\text{A } 2)$$

The forcing terms on the right-hand side of (A 1) are chosen to mimic the viscous stress (first term), and the unsteady dynamic pressure (second term). From the momentum equation (2.2), $\rho\partial u/\partial t \sim \nabla p$, one can see that an unsteady flow $G_0g(t)$ gives rise to such a pressure. An oscillating flow is specified by $g(t) = \exp(i\omega t)$.

The model is non-dimensionalized using the length scale \hat{R} and time scale \hat{R}/G_0 :

$$\frac{1 + \hat{\lambda}_\rho}{2}\hat{R}e\ddot{X} + \frac{1 + \hat{\lambda}}{2}\dot{X} + \hat{k}X = \frac{1 + \hat{\lambda}}{2}g(t) + \frac{1 + \hat{\lambda}_\rho}{2}\hat{R}e\dot{g}(t), \quad (\text{A } 3)$$

$$\dot{X}(0) = g(0), \quad X(0) = 0, \quad g(t) = \exp(it'\hat{S}t), \quad (\text{A } 4)$$

where the non-dimensional numbers are $\hat{R}e = \hat{\rho}\hat{R}G_0/\hat{\mu}$, $\hat{k} = \hat{\Gamma}/(\hat{\mu}G_0)$, $\hat{S}t = \omega\hat{R}/G_0$, and $t' = tG_0/\hat{R}$. The solution of this ODE is

$$X = \frac{(1 + \hat{\lambda}) + i(1 + \hat{\lambda}_\rho)\hat{R}e\hat{S}t}{2\hat{k} - (1 + \hat{\lambda}_\rho)\hat{R}e\hat{S}t^2 + i(1 + \hat{\lambda})\hat{S}t} \exp(it'\hat{S}t), \quad (\text{A } 5)$$

with a magnitude

$$|X| = \sqrt{\frac{(1 + \hat{\lambda})^2 + (1 + \hat{\lambda}_\rho)^2\hat{R}e^2\hat{S}t^2}{[2\hat{k} - (1 + \hat{\lambda}_\rho)\hat{R}e\hat{S}t^2]^2 + (1 + \hat{\lambda})^2\hat{S}t^2}}, \quad (\text{A } 6)$$

and a phase lag $\hat{\beta}$ behind the forcing [$X = |X|\exp i(t'\hat{S}t - \hat{\beta})$]:

$$\hat{\beta} = \tan^{-1} \frac{2\hat{S}t}{\hat{k}(1 + \hat{\lambda})} \left[\left(\frac{1 + \hat{\lambda}}{2} \right)^2 - \hat{k} \left(\frac{1 + \hat{\lambda}_\rho}{2} \right) \hat{R}e + \left(\frac{1 + \hat{\lambda}_\rho}{2} \right)^2 \hat{R}e^2\hat{S}t^2 \right]. \quad (\text{A } 7)$$

The system retains a natural frequency $\hat{S}t_n = \sqrt{2\hat{k}/[(1 + \hat{\lambda}_\rho)\hat{R}e]}$. From the solution (A 6), it is observed that as \hat{k} is varied, $|X|$ reaches a peak value and the system undergoes resonance when $\hat{S}t_n = \hat{S}t$. Note that this model is only qualitative, and may not quantitatively compare with the simulation. However, it contains the essential physics, and therefore describes the observed trends and various scalings.

REFERENCES

- BENTLEY, B. J. & LEAL, L. G. 1986 An experimental investigation of drop deformation and breakup in steady, two-dimensional linear flows. *J. Fluid Mech.* **167**, 241–283.
- BLAWZDZIEWICZ, J., CRISTINI, V. & LOEWENBERG, M. 2002 Critical behaviour of drops in linear flows. I. Phenomenological theory for drop dynamics near critical stationary states. *Phys. Fluids* **14**, 2709–2718.
- BLAWZDZIEWICZ, J., CRISTINI, V. & LOEWENBERG, M. 2003 Multiple stationary states for deformable drops in linear Stokes flow. *Phys. Fluids* **15**, L37–L40.
- BRADY, J. F. & ACRIVOS, A. 1982 The deformation and breakup of a slender drop in an extensional flow: inertial effects. *J. Fluid Mech.* **115**, 443–451.
- COX, R. G. 1969 The deformation of a drop in a general time-dependent fluid flow. *J. Fluid Mech.* **37**, 601–623.
- FRANKEL, N. A. & ACRIVOS, A. 1970 The constitutive equation for a dilute emulsion. *J. Fluid Mech.* **44**, 65–78.
- GRACE, H. P. 1982 Dispersion phenomena in high viscosity immiscible fluid systems and application of static mixers as dispersion devices in such systems. *Chem. Engng Commun.* **14**, 225–277.
- HAKIMI, F. S. & SCHOWALTER, W. S. 1980 The effects of shear and vorticity on deformation of a drop. *J. Fluid Mech.* **98**, 635–645.
- HINCH, E. J. & ACRIVOS, A. 1980. Long slender drops in a simple shear flow. *J. Fluid Mech.* **98**, 305–28.
- HOPFINGER, E. J., BROWAND, F. K. & GAGNE, Y. 1982 Turbulence and waves in a rotating tank. *J. Fluid Mech.* **125**, 505–534.
- KANG, I. S. & LEAL, L. G. 1987 Numerical solution of axisymmetric, unsteady free-boundary problems at finite Reynolds number I Finite-difference scheme and its application to the deformation of a bubble in uniaxial straining flow. *Phys. Fluids* **30**, 1929–1940.
- KANG, I. S. & LEAL, L. G. 1989 Numerical solution of axisymmetric, unsteady free-boundary problems at finite Reynolds number II Deformation of a bubble in biaxial straining flow. *Phys. Fluids A* **32**, 644–660.
- KANG, I. S. & LEAL, L. G. 1990 Bubble dynamics in time-periodic straining flows. *J. Fluid Mech.* **218**, 41–69.
- KENNEDY, M. R., POZRIKIDIS, C. & SKALAK, R. 1994 Motion and deformation of liquid drops and the rheology of dilute emulsions in simple shear flow. *Computers Fluids* **23**, 251–278.
- KHISMATULLIN, D. B., RENARDY, Y. & CRISTINI, V. 2003 Inertia-induced breakup of highly viscous drops subjected to simple shear. *Phys. Fluids* **15**, 1351–1354.
- LEGENDRE, D. & MAGNAUDET, J. 2003 Hydrodynamic interactions between two spherical bubbles rising side by side in a viscous liquid. *J. Fluid Mech.* **497**, 133–166.
- LI, J., RENARDY, Y. Y. & RENARDY, M. 2000 Numerical simulation of breakup of a viscous drop in simple shear flow through volume-of-fluid method. *Phys. Fluids* **12**, 269–282.
- LI, X. & SARKAR, K. 2005a Drop dynamics in an oscillating extensional flow at finite inertia. *Phys. Fluids* **17**, 027103.
- LI, X. & SARKAR, K. 2005b Rheology of a dilute emulsion of drops in finite Reynolds number oscillator extensional flows. *J. Non-Newtonian Fluid Mech.* **128**, 71–82.
- LI, X. & SARKAR, K. 2005c Effects of inertia on the rheology of a dilute emulsion of drops in shear. *J. Rheology* **49**, 1377–1394.
- LI, X. & SARKAR, K. 2005d Negative normal stress elasticity of emulsion of viscous drops at finite inertia. *Phys. Rev. Lett.* **95**, 256001.
- LOEWENBERG, M. & HINCH, E. J. 1996 Numerical simulation of a concentrated emulsion in shear flow. *J. Fluid Mech.* **321**, 395–419.
- MAGNAUDET, J. 2003 Small inertial effects on a spherical bubble, drop or particle moving near a wall in a time-dependent linear flow. *J. Fluid Mech.* **485**, 115–142.
- MAXWORTHY, T., HOPFINGER, E. J. & REDEKOPP, L. G. 1985 Wave motions on vortex cores. *J. Fluid Mech.* **151**, 141–165.
- NAVOT, Y. 1999 Critical behaviour of drop breakup in axisymmetric viscous flow. *Phys. Fluids* **11**, 990–996.
- RALLISON, J. M. 1980 A note on the time-dependent deformation of a viscous drop which is almost spherical. *J. Fluid Mech.* **98**, 625–633.

- RALLISON, J. M. 1981 A numerical study of the deformation and burst of a viscous drop in general shear flow. *J. Fluid Mech.* **109**, 465–482.
- RALLISON, J. M. 1984 The deformation of small viscous drops and bubbles in shear flows. *Annu. Rev. Fluid Mech.* **16**, 45–66.
- RAMASWAMY, S. & LEAL, L. G. 1997 A note on inertial effects in the deformation of Newtonian drops in uniaxial extensional flow. *Intl J. Multiphase Flow* **23**, 561–574.
- RENARDY, Y. & CRISTINI, V. 2001a Effects of inertia on drop breakup under shear. *Phys. Fluids* **13**, 7–13.
- RENARDY, Y. & CRISTINI, V. 2001b Scalings for fragments produced from drop breakup in shear flow with inertia. *Phys. Fluids* **13**, 2161–2164.
- RENARDY, Y., CRISTINI, V. & LI, J. 2002 Drop fragmentation distribution under shear with inertia. *Intl J. Multiphase Flow* **28**, 1125–1147.
- RISSO, F. & FABRE, J. 1998 Oscillations and breakup and a bubble immersed in a turbulent field. *J. Fluid Mech.* **372**, 323–355.
- SARKAR, K. & SCHOWALTER, W. R. 2000 Deformation of a two-dimensional viscoelastic drop at non-zero Reynolds number in time-periodic extensional flows. *J. Non-Newtonian Fluid Mech.* **95**, 315–342.
- SARKAR, K. & SCHOWALTER, W. R. 2001a Deformation of a two-dimensional drop at non-zero Reynolds number in time-periodic extensional flows: numerical simulation. *J. Fluid Mech.* **436**, 177–206.
- SARKAR, K. & SCHOWALTER, W. R. 2001b Deformation of a two-dimensional viscous drop in time-periodic extensional flows: analytical treatment. *J. Fluid Mech.* **436**, 207–230.
- SETH, K. S. & POZRIKIDIS, C. 1995 Effects of inertia on the deformation of liquid drops in simple shear flow. *Computers Fluids* **24**, 101–119.
- STOKES, Y. M. & TUCK, E. O. 2004 The role of inertia in extensional fall of a viscous drop. *J. Fluid Mech.* **498**, 205–225.
- STONE, H. A. 1994 Dynamics of drop deformation and breakup in viscous fluids. *Annu. Rev. Fluid Mech.* **26**, 65–102.
- STONE, H. A., BENTLEY, B. J. & LEAL, L. G. 1986 An experimental study of transient effects in the breakup of viscous drops. *J. Fluid Mech.* **173**, 131–158.
- TAYLOR, G. I. 1932 The viscosity of a liquid containing small drops of another liquid. *Proc. R. Soc. Lond. A* **138**, 41–48.
- TAYLOR, G. I. 1934 The formation of emulsions in definable fields of flow. *Proc. R. Soc. Lond. A* **146**, 501–523.
- TRYGGVASON, G., BUNNER, B., EBRAT, O. & TAUBAR, W. 1998 Computation of multiphase flows by a finite difference front tracking method. I. multi-fluid flows. *29th Computational Fluid Dynamics Lecture Series 1998-03*. Von Karman Institute of Fluid Dynamics, Sint-Genesius-Rode, Belgium.
- TRYGGVASON, G., BUNNER, B., ESMAEELI, A., JURIC, D., AL-RAWAHI, N., TAUBAR, W., HAN, J., NAS, S. & JAN, Y. J. 2001 A front-tracking method for the computations of multiphase flow. *J. Comp. Phys.* **169**, 708–759.
- TSAKALOS, V. T., NAVARD, P. & PEUVREL-DISDIER, E. 1998 Deformation and breakup mechanism of single drops during shear. *J. Rheol.* **42**, 1403–1417.
- YOUNGREN, G. K. & ACRIVOS, A. 1976 On the shape of a gas bubble in a viscous extensional flow. *J. Fluid Mech.* **76**, 433–442.